East Asian Journal on Applied Mathematics
doi: 10.4208/eajam.2023-040.050323

Vol. **xx**, No. x, pp. 1-23
xx 2023

Numerical Study of Fluid-Solid Interaction in Rotational Extrusion Flow

Yanan Zhou[1], Qiaolin He[1,*], Min Nie[2] and Changhua Yang[2]

[1]*School of Mathematics, Sichuan University, Chengdu 610064, China.*
[2]*Key Laboratory of Polymer Materials Engineering, Polymer Research Institute of Sichuan University, Chengdu 610065, China.*

Received 28 January 2023; Accepted (in revised version) 5 March 2023.

Abstract. The fluid particle dynamics method is employed to study the fluid-solid interaction problem, which can avoid the explicit implementation of fluid particle boundary condition and capture the hydrodynamic interaction well. We solve the incompressible Navier-Stokes equation coupled with the rigid body motion equation in polar or cylindrical coordinates. A pressure stabilization scheme is used to solve the system in polar coordinates for two dimensional case and cylindrical coordinates for three dimensional case. Our objective is to understand numerically the fluid-solid interaction in rotational extrusion flow. We numerically verify the correctness of method presented here and give comparative analysis for different parameters. We present the Jeffery orbit formulation in annular region. Numerical experiments show that the fluid particle dynamics method is reliable and efficient for numerical simulation of particulate flow in cylindrical coordinate system.

AMS subject classifications: 76-10

Key words: Fluid particle dynamics method, cylindrical coordinates, incompressible Navier-Stokes, finite difference, repulsive force.

1. Introduction

The coupling of fluid-solid mechanics is a branch of mechanics generated by the intersection of fluid and solid mechanics. Its important feature is the interaction between two-phase media, including the deformation or movement of solid structure under the action of fluid load, and the influence of solid deformation or movement on flow field. It is the interaction between fluid and solid structure that produces various fluid-solid coupling phenomena under different conditions. In fact, such problems appear in various areas, including strong wind swing in high-rise buildings construction [18,21], interaction between blood and heart in bioengineering [27], complex stress and temperature experienced by

*Corresponding author. *Email addresses:* zyn980228@163.com (Y. Zhou), qlhejenny@scu.edu.cn (Q. He), poly.nie@gmail.com (M. Nie), yangchanghua18@163.com (C. Yang)

high molecular polymers during processing [2, 17], etc. Therefore, numerical simulations of fluid-solid coupling is of great importance. However, researchers rarely focus on the problem of fluid-solid interactions when multiple particles are subjected to rotational extrusion in cylindrical instruments. In this paper, we want to explain and validate part of the work of the rotary extrusion rheometer – a machine that studies the rheological behavior of polymers – by studying the fluid-structure interaction in a hollow cylinder.

There are many numerical simulation methods for the coupling problem of incompressible viscous fluid and solid particles e.g. arbitrary Lagrangian-Eulerian method (ALE), fictitious domain method (FDM), immersed boundary method (IBM), and fluid particle dynamics (FPD) method. The ALE method directly simulating the motion of fluid and particles is based on moving unstructured grids. It needs remeshing and projection [12, 13]. The fictitious domain method extends the actual computational domain inside or outside of the desired object to form a fictitious computational domain with a simple shape, so that a structured grid can be used to solve it efficiently [8]. The fictitious domain method has evolved different algorithms according to different problems. The distributed Lagrange multiplier method is proposed in [7]. The immersed boundary method, introduced by Peskin and McQueen [26], is widely used in fluid and solid simulations. It uses non-boundary-conforming meshes in numerical discretization, and the no-slip condition on the surface of the immersed object is enforced by adding a volume force to the momentum equation. The FPD method was proposed by Tanaka and Araki [24]. It is a diffusion interface method, which can avoid the explicit implementation of fluid-solid boundary condition and capture the hydrodynamic interaction well. This method has efficient numerical simulation performance, and has been well verified by numerical experiments [25].

In 2005, the effect of particle size on the lateral migration of particles in rectangular microchannels with different nozzle shapes at low Reynolds numbers was studied by Staben *et al.* [22]. The particle loaded flow in two-dimensional channels was studied in [3] using the direct numerical simulation method of coupling Navier-Stokes equation and particle motion equation. In 2008, the motion of elliptical particles with neutral buoyancy in three-dimensional Poiseuille flow and the rotation and orientation characteristics of particles were studied in [20] using the fictitious domain method based on Lagrangian multipliers. Nourbakhsh *et al*. [19] studied the movement of three-dimensional deformable droplets in the plane Poiseuille flow by a finite difference/interface tracking method. Kim *et al.* [16] investigated lateral migration of three-dimensional elastic capsules under the plane Poiseuille flow by the penalty immersion boundary method.

In this paper, we use FPD method to study the interaction between fluid and solid in cylinder coordinates, which has two important features [4], viz.

(1) The particle is approximated as a highly viscous fluid.

(2) The viscosity profile is described by a smooth interface profile function.

Approximation (1) makes the method free from the solid-fluid boundary condition, significantly simplifies the treatment of many-body hydrodynamic interactions while satisfying the incompressible condition without the Stokes approximation. Approximation (2) allows to incorporate an extra degree of freedom in a fluid. Therefore, the Navier-Stokes

equation can be solved uniformly in the fluid and solid regions, avoiding the realization of boundary conditions and the case of large number of particles. It greatly reduces the complexity of method without explicitly solving the phase field equation. In our work, we solve the Navier-Stokes equation in the sense of polar coordinates and cylindrical coordinates. Therefore, the computational domain is a regular rectangle or cuboid. Meanwhile more calculations of position and orientation of the rigid body are needed when the reference coordinate system is changed. The finite difference discretization in staggered marker-and-cell (MAC) grid is used in space. To obtain the motion of a rigid body in an incompressible fluid, we update the translational and angular velocities describing the rigid body, according to the solution obtained from Navier-Stokes equation. In the two dimensional case, we present Jeffery orbit equation in annular region in polar coordinates.

The rest of the paper is organized as follows. In Section 2, we introduce FPD method for the system composed of Navier-Stokes equation and particle motion equation in cylindrical coordinates. A stabilized time discretization and finite difference scheme are employed. Numerical verification and analysis in two dimensions are given and the numerical experiments presented in Section 3 deal with the particulate flow in rotational extrusion flow. Section 4 contains a few final remarks.

2. Mathematical Methods

2.1. Fluid particle dynamics method

The FPD method is a hybrid method [28,29], in which rigid bodies are approximated as non-deformable, highly viscous fluid particles with a viscosity η_s much larger than the fluid viscosity η_l. Two sets of variables are employed — viz. on-lattice variables including the velocity field $\vec{u}(\vec{x})$, the pressure field $p(\vec{x})$, the composition field $\phi(\vec{x})$, and the viscosity field $\eta(\vec{x})$, and off-lattice variables, including the particle's center of mass position $\mathbf{G}_j$, the particle's orientation $d(\vec{x})$, the particle's center-of-mass velocity $\vec{V}_j$, and the particle's angular velocity $\vec{\omega}_j$. The density of rigid body and fluid may be different. The densities are obtained when the position of the particle's is updated. For simplicity, we assume that the corresponding densities are equal to ρ.

The Reynolds number is defined by $Re = \rho UD/\eta_l$, where U is characteristic velocity and D characteristic length. Since the solid is approximated by a highly viscous fluid, the velocity field can be obtained by solving the dimensionless Navier-Stokes equation (2.1) in the whole domain Ω,

$$\begin{aligned} &\mathrm{Re}\left[\frac{\partial \vec{u}}{\partial t} + (\vec{u}\cdot\nabla)\vec{u}\right] + \nabla p = \nabla\cdot\left[\eta\left(\nabla\vec{u} + \nabla\vec{u}^t\right)\right] + \vec{f} \quad \text{in } \Omega, \\ &\nabla\cdot\vec{u} = 0 \qquad\qquad\qquad\qquad\qquad\qquad\qquad\qquad\qquad\quad \text{in } \Omega, \end{aligned} \tag{2.1}$$

where $\vec{f}$ is the external force. The position of the rigid body can be determined by its orientation $d(\vec{x})$ and the center of mass position $\mathbf{G}_j$, or by the composition field

$$\phi(\vec{x}) = \frac{1}{2}\left\{\tanh\left[\frac{d(\vec{x})}{\xi}\right] + 1\right\},$$

where ξ is a small length scale characterizing the fluid-solid interfacial thickness and $d(\vec{x})$ is the signed distance to the fluid-solid interface, which is positive inside and negative outside the solid body. This means $\phi = 1$ in the solid region and $\phi = 0$ in the fluid region. At the interface between fluid and solid, there is a transition layer with $0 < \phi < 1$. The thickness of this transition layer is determined by ξ. There are several different definitions of viscosity. Here we use the linear interpolation function from [24], viz.

$$\eta(\phi) = (1-\phi)\eta_l + \phi\eta_s,$$

which corresponds to a non-slip fluid-solid boundary condition. Therefore, we obtain $\eta = \eta_s$ inside the solid body, $\eta = \eta_l$ outside the body and $\eta_l < \eta < \eta_s$ in the transition layer. We define the viscosity ratio $R_\eta = \eta_s/\eta_l$. In the reference [25], it is shown that the flow will not enter the inside of the solid and the flow pattern is similar to that around the solid when $R_\eta = 50$. In addition, the size of the particle's should be large enough for the interface thickness, which is the general requirement of diffusion interface method. Once these criteria are satisfied, the flow within the solid region is almost the same as that within an exact rigid body. Therefore, the average velocity $\vec{u}(\vec{x})$ in the particle's area can be taken as the translational velocity $\vec{V}_j$ of the particle, and the average of flow angular velocity

$$\vec{v} \equiv \frac{1}{2}\nabla \times \vec{u}$$

can be used to calculate the angular velocity $\vec{\omega}_j$ of the particle.

The general algorithm of the FPD method is stated as follows: Given initial conditions of the particle's center-of-mass position $\mathbf{G}_j^0$, orientation $d_j^0(\vec{x})$ and flow field $\vec{u}^0(\vec{x})$. Assuming that $\mathbf{G}_j^n$, $d_j^n(\vec{x})$ and $\vec{u}^n(\vec{x})$ are known, at the time-step n we proceed as follows:

Step 1. Calculate the composition field $\phi^n(\vec{x})$ and viscosity field $\eta^n(\phi^n)$.

Step 2. Solve Navier-Stokes equation and obtain $\vec{u}^{n+1}(\vec{x})$.

Step 3. Calculate the particle's center-of-mass velocity $\vec{V}_j^n$ and angular velocity $\vec{\omega}_j^n$ by

$$\begin{aligned} \vec{V}_j^n &= \int \phi(\vec{x})\vec{u}^n(\vec{x})\mathrm{dV}\left(\int \phi(\vec{x})\mathrm{dV}\right)^{-1}, \\ \vec{\omega}_j^n &= \int \phi(\vec{x})\vec{v}^n(\vec{x})\mathrm{dV}\left(\int \phi(\vec{x})\mathrm{dV}\right)^{-1}. \end{aligned} \tag{2.2}$$

Step 4. Update the particle's center-of-mass position $\mathbf{G}_j^{n+1}$ and orientation $d_j^{n+1}(\vec{x})$

$$\begin{aligned} \mathbf{G}_j^{n+1} &= \mathbf{G}_j^n + \Delta t\vec{V}_j^n, \\ d_j^{n+1}(\vec{x}) &= d_j^n(\vec{x}) + \Delta t\vec{\omega}_j^n \times d_j^n(\vec{x}). \end{aligned}$$

Step 5. Let $n = n+1$ and go to Step 1.

Now we consider the collision between rigid body and boundary or between rigid bodies. We assume that the collision is smooth — i.e. at the contact point the velocities of rigid bodies coincide. The only preventive measure that needs to be taken is to avoid the overlap of rigid body occupied areas [5,7]. In order to achieve this goal, we make adjustments in Step 3 by introducing an intermediate variable $\vec{V}_j^{*n}$, $\vec{\omega}_j^{*n}$ and the repulsive force $\mathbf{F}_j$.

Firstly, the central velocity and the angular velocity of rigid body are calculated by

$$\begin{aligned}\vec{V}_j^{*n} &= \int \phi(\vec{x})\vec{u}^n(\vec{r})\mathrm{dV}\left(\int \phi(\vec{x})\mathrm{dV}\right)^{-1},\\ \vec{\omega}_j^{*n} &= \int \phi(\vec{x})\vec{v}^n(\vec{r})\mathrm{dV}\left(\int \phi(\vec{x})\mathrm{dV}\right)^{-1}.\end{aligned} \tag{2.3}$$

Secondly, the equations for rigid body motion are

$$\begin{aligned}M_j\frac{\vec{V}_j^n-\vec{V}_j^{*n}}{\Delta t} &= \mathbf{F}_j,\\ \mathbf{I}_j\frac{\vec{\omega}_j^n-\vec{\omega}_j^{*n}}{\Delta t}+\vec{\omega}_j^{*n}\times\mathbf{I}_j\vec{\omega}_j^{*n} &= \mathbf{T}_j,\end{aligned} \tag{2.4}$$

where M_j is the mass of the j-th rigid body, $\mathbf{I}_j$ the inertia tensor of the j-th rigid body, $\mathbf{F}_j$ a short range repulsive force acting on the j-th rigid body introduced to avoid the overlap of the rigid body occupied areas, and $\mathbf{T}_j$ the torque of the repulsive force $\mathbf{F}_j$ acting on the j-th rigid body. The definitions of repulsive force $\mathbf{F}_j$ and torque $\mathbf{T}_j$ are given in [6, Appendix A]. Then we make a cycle in Steps 3 and 4 of the FPD algorithm until the repulsive force $\mathbf{F}_j$ between rigid body and the boundary or between the rigid bodies becomes zero.

2.2. Navier-Stokes equation solver

In this paper, we solve the Navier-Stokes equation (2.1) in cylindrical coordinates. The finite difference discretization is used in space. In cylindrical domain,

$$\Omega=\left\{(r,\theta,z)\mid 0\le r\le R,\ 0\le\theta\le 2\pi,\ 0\le z\le L\right\},$$

we have

$$\begin{aligned}\nabla &= \left(\frac{\partial}{\partial r},\frac{1}{r}\frac{\partial}{\partial\theta},\frac{\partial}{\partial z}\right),\\ \nabla^2 &= \frac{1}{r}\frac{\partial}{\partial r}\left(r\frac{\partial}{\partial r}\right)+\frac{1}{r^2}\frac{\partial^2}{\partial\theta^2}+\frac{\partial^2}{\partial z^2},\\ \nabla\cdot\vec{u} &= \frac{1}{r}\frac{\partial(ru_r)}{\partial r}+\frac{1}{r}\frac{\partial u_\theta}{\partial\theta}+\frac{\partial u_z}{\partial z}.\end{aligned}$$

2.2.1. Time-discretization

We solve Navier-Stokes equation by a numerical method based on the pressure stabilization scheme in [9]. The divergence free condition is replaced by

$$\nabla\cdot\vec{u}-\tau\nabla^2 p_t=0,$$

where τ is a small parameter and p_t is the time derivative of the pressure. For simplicity, we assume $\vec{f}=0$. Given the initial condition $\vec{u}^0$ and $p^{-1}=p^0=0$, we compute $\vec{u}^{n+1}$ firstly and then solve p^{n+1}. For $n\geq 0$, and $(r,\theta,z)\in\Omega$, the semi-implicit scheme is

$$\begin{aligned}
&\mathrm{Re}\left[\frac{\vec{u}^{n+1}-\vec{u}^n}{\Delta t}+(\vec{u}^n\cdot\nabla)\vec{u}^{n+1}+\frac{1}{2}(\nabla\cdot\vec{u}^n)\vec{u}^{n+1}\right]\\
&=-\nabla\left(2p^n-p^{n-1}\right)+\nabla\cdot\left[\eta^{n+1}D\left(\vec{u}^{n+1}\right)\right],\\
&\nabla^2\left(p^{n+1}-p^n\right)=\frac{1}{\Delta t}\mathrm{Re}\,\nabla\cdot\vec{u}^{n+1}.
\end{aligned}$$

For $n\geq 2$, the semi-implicit scheme is

$$\begin{aligned}
&\mathrm{Re}\left[\frac{3\vec{u}^{n+1}-4\vec{u}^n+\vec{u}^{n-1}}{2\Delta t}+\left(\vec{u}^{*,n+1}\cdot\nabla\right)\vec{u}^{n+1}\right]\\
&=-\nabla\left(p^n+\frac{4}{3}\psi^n-\frac{1}{3}\psi^{n-1}\right)+\nabla\cdot\left[\eta^{n+1}D\left(\vec{u}^{n+1}\right)\right],\\
&\nabla^2\psi^{n+1}=\frac{3}{2\Delta t}\mathrm{Re}\,\nabla\cdot\vec{u}^{n+1},\\
&p^{n+1}=p^n+\psi^{n+1}-\eta^{n+1}\nabla\cdot\vec{u}^{n+1},
\end{aligned}$$

where $(\cdot)^{*,n+1}=2(\cdot)^n-(\cdot)^{n-1}$, $\psi^n=p^n-p^{n-1}$, and $D(\vec{u})=\nabla\vec{u}+\nabla\vec{u}^t$.

2.2.2. Space-discretization

The finite difference scheme on a uniformly MAC grid [11] is employed in the computational domain Ω, where the pressure p is discretized on an integer grid, while the velocity components u_r,u_θ,u_z are defined on the half-integer grid $p(i,j,k),u_r(i+1/2,j,k),u_\theta(i,j+1/2,k)$, and $u_z(i,j,k+1/2)$, cf. Fig. 1. The structure of the staggered MAC grid is consistent

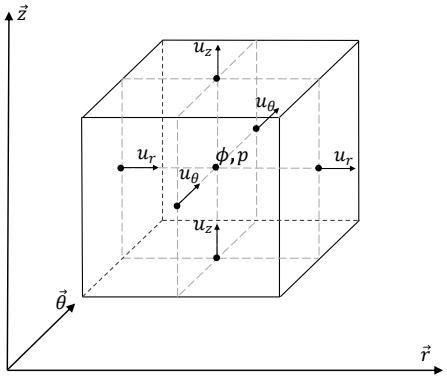

Figure 1: Staggered grids.

with the central difference scheme, which enables the decoupling of velocity and pressure, bringing great convenience and precision to computation [29]. The discretization of the differential operator is shown in Appendix B.

2.3. Calculation of position and orientation of the rigid body

The standard ellipsoid equation in three dimensions is

$$\frac{x_1^2}{a^2}+\frac{y_1^2}{b^2}+\frac{z_1^2}{c^2}=1,$$

where ellipsoid and coordinate axes are parallel. We use this equation in order to describe the ellipsoid equation after motion. We call the real Cartesian coordinate system $O-x_1y_1z_1$ as the source coordinate system, and the final coordinate system $O-x_2y_2z_2$ as the target coordinate system. The source coordinate system should be transformed to the target coordinate system through a coordinate transformation. We first consider the rotation transformation as shown in Fig. 2.

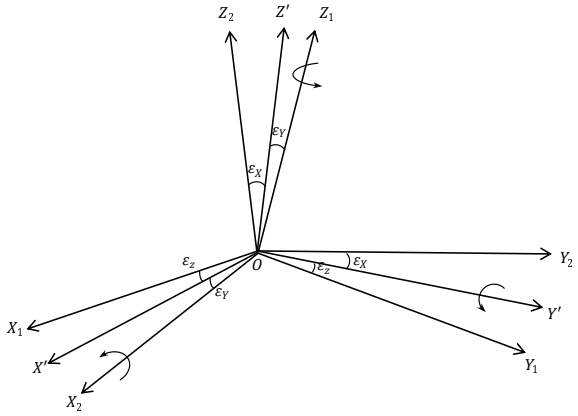

Figure 2: 3D coordinate rotation transformation.

We can achieve the conversion from $O-X_1Y_1Z_1$ to $O-X_2Y_2Z_2$ through three rotations

$$\begin{bmatrix} X_2 \\ Y_2 \\ Z_2 \end{bmatrix} = R(\varepsilon)\begin{bmatrix} X_1 \\ Y_1 \\ Z_1 \end{bmatrix},$$

where

$$R(\varepsilon)=R_1(\varepsilon_X)R_2(\varepsilon_Y)R_3(\varepsilon_Z),$$

and

$$R_1(\varepsilon_X)=\begin{bmatrix} 1 & 0 & 0 \\ 0 & \cos\varepsilon_X & \sin\varepsilon_X \\ 0 & -\sin\varepsilon_X & \cos\varepsilon_X \end{bmatrix},\quad R_2(\varepsilon_Y)=\begin{bmatrix} \cos\varepsilon_Y & 0 & -\sin\varepsilon_Y \\ 0 & 1 & 0 \\ \sin\varepsilon_Y & 0 & \cos\varepsilon_Y \end{bmatrix},$$

$$R_3(\varepsilon_Z) = \begin{bmatrix} \cos\varepsilon_Z & \sin\varepsilon_Z & 0 \\ -\sin\varepsilon_Z & \cos\varepsilon_Z & 0 \\ 0 & 0 & 1 \end{bmatrix}.$$

In our experiment, we should additionally consider the relationship between Cartesian coordinate and cylindrical coordinate — i.e. the angle ε_0 involved in Fig. 3.

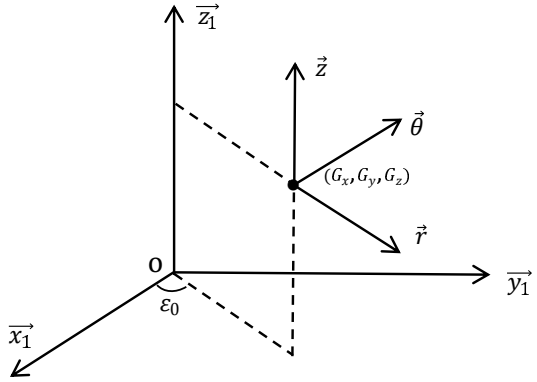

Figure 3: Schematic of coordinate transformation.

The transformation from the source coordinate system to the target coordinate system in the experiment is as follows:

$$\begin{bmatrix} x_2 \\ y_2 \\ z_2 \end{bmatrix} = R_3(-\varepsilon_0) R(\varepsilon_{change}) R_3(\varepsilon_0) \begin{bmatrix} x_1 \\ y_1 \\ z_1 \end{bmatrix},$$

where $R(\varepsilon_{change}) = R_1(\varepsilon_r)R_2(\varepsilon_\theta)R_3(\varepsilon_z)$, the ε_r denotes the rotational angle of the rigid body relative to the $\vec{r}$ axis, the ε_θ denotes the rotational angle of the rigid body relative to the $\vec{\theta}$ axis and the ε_z denotes the rotational angle of the rigid body relative to the $\vec{z}$ axis. And ε_r, ε_θ and ε_z can be calculated by Eq. (2.2). Then the space position equation of the ellipsoid rigid body can be written as

$$\frac{(x_2 - G_x)^2}{a^2} + \frac{(y_2 - G_y)^2}{b^2} + \frac{(z_2 - G_z)^2}{c^2} = 1,$$

where (G_x, G_y, G_z) is the position coordinate of the center of mass of the rigid body in the source space, so that the position information of the rigid body can be determined.

3. Numerical Experiments

We firstly verify the reliability of the scheme presented in the above section. Secondly, we study the fluid-solid interaction in the annular region in two dimension and then we simulate the fluid-solid interaction in rotational extrusion flow in three dimension.

3.1. Steady spiral flow

We consider the Couette flow between two concentric rings as shown in Fig. 4.

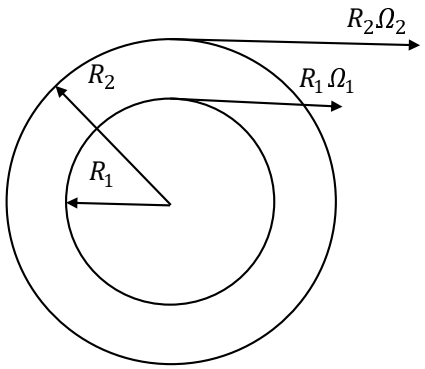

Figure 4: Schematic of Couette flow in slit between two concentric rings.

Assuming that the inner wall speed is Ω_1 and the outer wall speed $\Omega_2 = 0$, the fluid is driven by the rotation of the inner wall and there is no slip on the wall. Then the maximum velocity on the inner wall is $u_\theta = R_1\Omega_1$, the minimum velocity on the outer wall is $u_\theta = 0$, and the velocity at any radius is $\vec{u} = (0, u_\theta(r))$.

According to [1], the driving force for fluid motion is generated by the rotation of the wall — i.e.

$$\frac{1}{r^2}\frac{\partial\left(r^2\tau_{r\theta}\right)}{\partial r} = 0.$$

The shear stress $\tau_{r\theta} = c/r^2$ is introduced, where c is the integral constant. Furthermore, for power-law fluids, we have

$$\tau_{r\theta} = \frac{c}{r^2} = K\left[r\frac{d}{dr}\left(\frac{u_\theta}{r}\right)\right]^n,$$

where K is a constant. It is easy to obtain that any velocity of the fluid along the radial direction in the flow field generated by the inner wall rotation can be expressed as

$$u_\theta(\mathrm{r}) = r\Omega_1\frac{1-(R_2/r)^{2/n}}{1-(R_1/R_2)^{-2/n}}.$$

For comparison, as in Fig. 4, the computational domain is

$$\Omega = \left\{(r,\theta) \mid R_1 \le r \le R_2,\ 0 \le \theta \le 2\pi\right\}.$$

In polar coordinates, we have

$$\nabla = \left(\frac{\partial}{\partial r}, \frac{1}{r}\frac{\partial}{\partial\theta}\right),$$
$$\nabla^2 = \frac{1}{r}\frac{\partial}{\partial r}\left(r\frac{\partial}{\partial r}\right) + \frac{1}{r^2}\frac{\partial^2}{\partial\theta^2},$$
$$\nabla\cdot\vec{u} = \frac{1}{r}\frac{\partial\left(ru_r\right)}{\partial r} + \frac{1}{r}\frac{\partial u_\theta}{\partial\theta}.$$

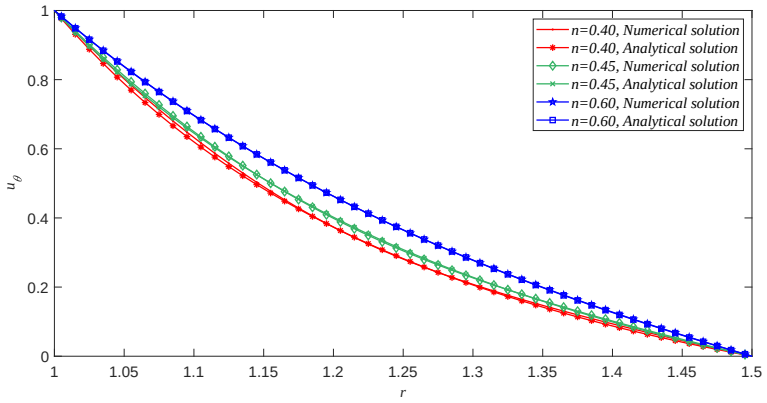

Figure 5: Numerical and analytical solutions for power law exponent, n=0.4, n=0.45 and n=0.6.

We choose the Bird-Carreau model as the constitutive equation of the power-law fluid [23]

$$\eta = \eta_\infty + (\eta_0 - \eta_\infty)\left[1 + (\lambda\dot{\gamma})^2\right]^{(n-1)/2},$$

where the strain tensor $\dot{\gamma} = D(\vec{u}) : D(\vec{u})$, $\eta_0 = 7\eta_\infty$, $\lambda = 0.6$, $R_1 = 1.0$, $R_2 = 1.5$ and $\Omega_1 = 1$, the numerical solution of the power-law exponent at $n = 0.4, n = 0.45$ and $n = 0.6$ are obtained. The comparisons are shown in Fig. 5 to illustrate the reliability of the Navier-Stokes solver. It is easily seen that the analytical solution is consistent with the numerical solution.

3.2. Simulation in two dimension

We consider two dimensional computation in two concentric rings as shown in Fig. 4. The drag coefficient is defined as $C_D = \mathbf{F}/\mathbf{V}$ [28], where $\mathbf{F}$ is a constant external force and $\mathbf{V}$ is the steady velocity of the rigid body under the drag of the force. We simulate constant force $\mathbf{F}$ dragging rigid particles under periodic boundary conditions. The parameters fluid viscosity $\eta_l = 0.00001, R_1 = 4.75, R_2 = 5.75, a = b = 10.0/100$, when the rotation speed is positive, the fluid moves counterclockwise. The mesh grid is $nr \times n\theta = 100, 150, 200 \times 3000$, the time step is $\Delta t = 0.01dr$. The influence of Reynolds number on the drag coefficient is shown in Fig. 6. The drag coefficient is goes to a constant as *Re* varies from 1 to 100 for a fixed force. The case that we consider is different from the benchmark where the particle is dragged by a constant external force along x-axis [10], but the overall results are similar.

Next, we consider the Jeffery orbit in the annular region. We place the rigid body particle as shown in Fig. 7. The Reynolds number Re $= 1.0$, the fluid viscosity $\eta_l = 0.001, R_\eta = 100$, the long and short axes of the elliptic rigid body are $a = 18.0/100$, $b = 9.0/100$ respectively, and the interface thickness $\xi = 0.9/100$. The parameters $R_1 = 0.75, R_2 = 1.75, R_1\Omega_1 = 2.0$ and $R_2\Omega_2 = 2.0$. The mesh grid is $nr \times n\theta = 100 \times 620$, the time step is $\Delta t = 0.01dr$. The boundary condition is

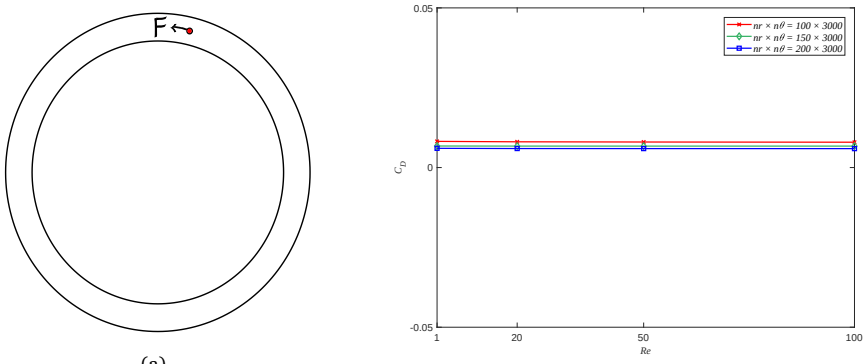

(a) (b)

Figure 6: (a) Circular rigid body particle with radius 10.0/100 is dragged by constant force $\mathbf{F} = 0.1$; (b) The influence of different Reynolds number on drag coefficient with three different mesh grid.

$$
\begin{aligned}
&u_r(R_1) = 0, && u_\theta(R_1) = R_1\Omega_1 && \text{on } r = R_1,\\
&u_r(R_2) = 0, && u_\theta(R_2) = -R_2\Omega_2 && \text{on } r = R_2,\\
&u_r(0) = u_r(2\pi), && u_\theta(0) = u_\theta(2\pi) && \text{on } \theta = 0, \quad \theta = 2\pi,\\
&\left.\frac{\partial p}{\partial \mathbf{n}}\right|_{\partial\Omega} = 0 && && \text{on } (r,\theta) \in \partial\Omega,
\end{aligned}
$$

which represents the inner and outer walls rotating inversely similarly like shear motion. Fig. 8 shows the fluid structure interaction for different R_η in the shear flow field, and we get the similar results as in [25]. Jeffery [14], presented the following relation between the angular velocity ω of the elliptic particle rotation and the current angle θ of the particle

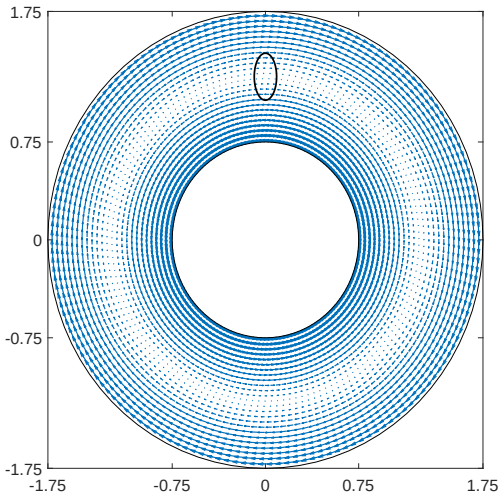

Figure 7: A particle in annular region.

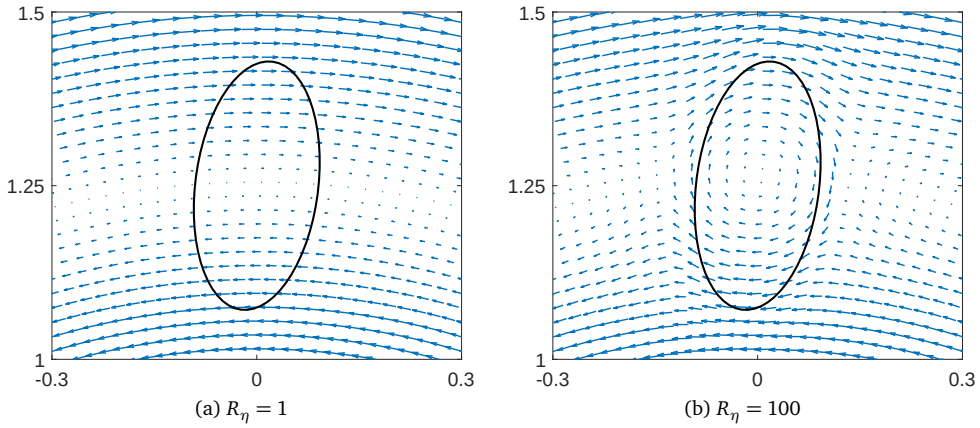

(a) $R_\eta = 1$ (b) $R_\eta = 100$

Figure 8: Flow field around a particle under shear field: (a)$R_\eta = 1$, (b)$R_\eta = 100$.

under the shear of Stokes equation

$$\omega = \frac{\dot{\gamma}}{2}[-1 + P\cos(2\theta)],$$

where $\dot{\gamma}$ is the shear rate of shear flow, θ is the angular orientation of the elliptic particle, $P = (1-e^2)/(1+e^2)$, and e is the axial ratio. Fig. 9 shows the relationship between the angular velocity of the rigid body and the angle of rotation in our case. The fitting function in Fig. 9 has the form

$$\omega = \frac{\dot{\gamma}^{'}}{2}[0.45 + P^{'}\cos(2\theta)],$$

where $\dot{\gamma}^{'} = -(R_1\Omega_1 + R_2\Omega_2)/(R_2 - R_1)$, and $P^{'} = 1.25P$. Our numerical experiment is not carried out in a real rectangular shear flow but we can still see that our numerical results

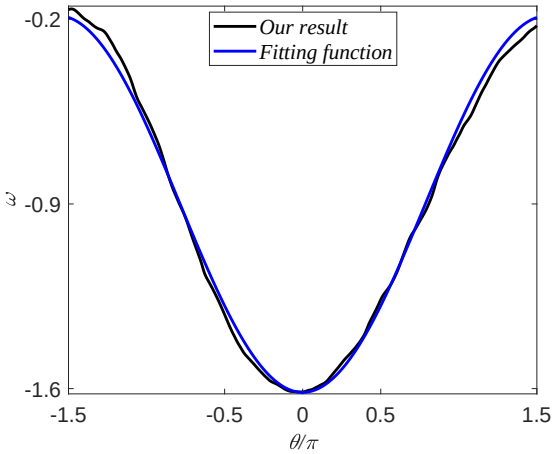

Figure 9: Relationship between angular velocity ω of elliptic particle and the angular orientation θ.

have similar trigonometric function shapes with the Jeffery orbit. These results validate our fluid structure coupling solver.

3.3. Simulation in three dimension

We consider a hollow cylinder with inner radius R_1, outer radius R_2 and the length L, cf. Fig. 10. The calculational domain is

$$\Omega = \{(r,\theta,z) \mid R_1 \le r \le R_2,\ 0 \le \theta \le 2\pi,\ 0 \le z \le L\}.$$

Note that the Reynolds number $Re = 1.0$, the fluid viscosity $\eta_l = 0.001, R_\eta = 100$, the ellipsoid rigid body axis lengths are $a = 15/128$, $b = 10/128$, $c = 9/128$ and interface thickness $\xi = 0.9/128$. The parameters $R_1 = 1.0, R_2 = 1.5, R_1\Omega_1 = 15, R_2\Omega_2 = 15$ and $L = 6.5$, when the rotation speed is positive, the fluid flows counterclockwise. The mesh size is $nr \times n\theta \times nz = 32 \times 380 \times 410$, the time step $\Delta t = 0.01dr$. For velocity, the Dirichlet boundary is used in r direction, the periodic boundary condition is used in θ direction and zero Neumann boundary condition in the z direction is applied. The boundary conditions for pressure are [15]

$$\begin{aligned} &\frac{\partial p}{\partial \mathbf{n}} = 0 && \text{on } (r,\theta) \in \partial\Omega, \\ &p(0) = p_{in}, \quad p(L) = p_{out} && \text{on } z = 0, \quad z = L, \end{aligned}$$

where p_{in} and p_{out} are the pressure values at the inlet and outlet of the hollow cylinder. We take $p_{in} = 6.0$ and $p_{out} = 0$ here. There are four different boundary conditions of velocity according to different rotation modes as shown in Table 1, which include that inner wall and outer wall both rotate in the same direction or in the opposite direction, or one of walls does not rotate.

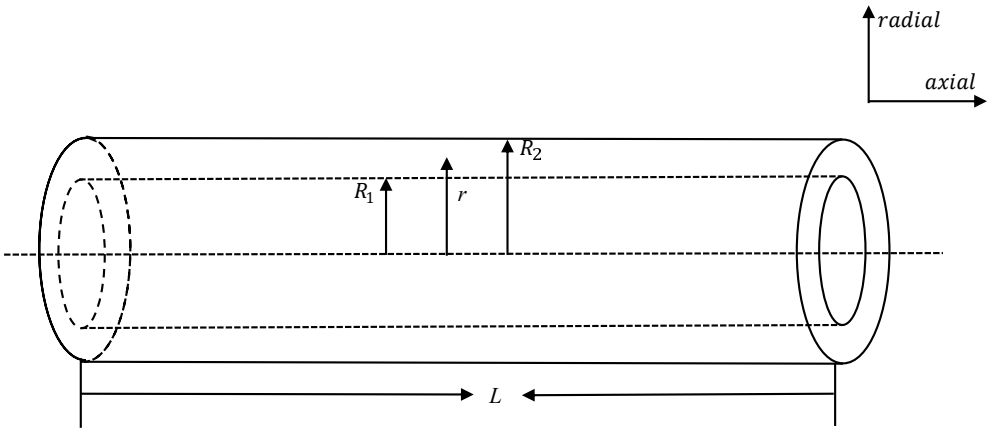

Figure 10: Hollow cylinder.

Table 1: Boundary conditions of different rotation modes in 3D.

	3D(I)	**3D(II)**	**3D(III)**	**3D(IV)**
on $\mathbf{r = R_1}$	$u_r(R_1) = 0$	$u_r(R_1) = 0$	$u_r(R_1) = 0$	$u_r(R_1) = 0$
	$u_\theta(R_1) = R_1\Omega_1$	$u_\theta(R_1) = 0$	$u_\theta(R_1) = R_1\Omega_1$	$u_\theta(R_1) = R_1\Omega_1$
	$u_z(R_1) = 0$	$u_z(R_1) = 0$	$u_z(R_1) = 0$	$u_z(R_1) = 0$
on $\mathbf{r = R_2}$	$u_r(R_2) = 0$	$u_r(R_2) = 0$	$u_r(R_2) = 0$	$u_r(R_2) = 0$
	$u_\theta(R_2) = 0$	$u_\theta(R_2) = R_2\Omega_2$	$u_\theta(R_2) = R_2\Omega_2$	$u_\theta(R_2) = -R_2\Omega_2$
	$u_z(R_2) = 0$	$u_z(R_2) = 0$	$u_z(R_2) = 0$	$u_z(R_2) = 0$
on $\theta = \mathbf{0}$	$u_r(0) = u_r(2\pi)$	$u_r(0) = u_r(2\pi)$	$u_r(0) = u_r(2\pi)$	$u_r(0) = u_r(2\pi)$
and	$u_\theta(0) = u_\theta(2\pi)$	$u_\theta(0) = u_\theta(2\pi)$	$u_\theta(0) = u_\theta(2\pi)$	$u_\theta(0) = u_\theta(2\pi)$
on $\theta = \mathbf{2}\pi$	$u_z(0) = u_z(2\pi)$	$u_z(0) = u_z(2\pi)$	$u_z(0) = u_z(2\pi)$	$u_z(0) = u_z(2\pi)$
on $\mathbf{z = 0}$	$\partial u_r/\partial \mathbf{n} = 0$	$\partial u_r/\partial \mathbf{n} = 0$	$\partial u_r/\partial \mathbf{n} = 0$	$\partial u_r/\partial \mathbf{n} = 0$
and	$\partial u_\theta/\partial \mathbf{n} = 0$	$\partial u_\theta/\partial \mathbf{n} = 0$	$\partial u_\theta/\partial \mathbf{n} = 0$	$\partial u_\theta/\partial \mathbf{n} = 0$
on $\mathbf{z = L}$	$\partial u_z/\partial \mathbf{n} = 0$	$\partial u_z/\partial \mathbf{n} = 0$	$\partial u_z/\partial \mathbf{n} = 0$	$\partial u_z/\partial \mathbf{n} = 0$

3.3.1. Stable rotational extrusion flow

Firstly we discuss the fully developed flow field with boundary condition 3D(I). In Fig. 11, we present the distribution of the annular velocity u_θ with respect to radial $\vec{r}$ at the section $z = 3.0$ and the axial velocity u_z with respect to radial $\vec{r}$ at the section $\theta = \pi$. Due to the existence of pressure difference between the inlet and outlet and the non-slip boundary condition of the axial velocity u_z on the cylinder wall, the flow field distribution of a section of u_z at $\theta = \pi$ looks like a parabola, which is similar to the Poiseuille flow. The annular velocity u_θ in a section of $z = 3.0$ is similar to that in a two-dimensional ring, and the flow field distribution is similar to the shear flow, while the radial velocity u_r is close to zero.

3.3.2. Fluid-rigid body interaction in rotational extrusion flow

We present three-dimensional simulations of fluid-rigid body interaction with four different boundary conditions. For simplicity, we set the initial velocity $u_\theta = -30.0 \times r + 45.0$ and $u_z = 32.0 \times (r - 1.0) \times (1.5 - r)$ with boundary condition 3D(I), $u_\theta = 30.0 \times r - 30.0$ and $u_z = 32.0 \times (r - 1.0) \times (1.5 - r)$ with boundary condition 3D(II), $u_\theta = 15.0$ and $u_z = 32.0 \times (r - 1.0) \times (1.5 - r)$ with boundary condition 3D(III) and $u_\theta = -60.0 \times r + 75.0$ and $u_z = 32.0 \times (r - 1.0) \times (1.5 - r)$ with boundary condition 3D(IV). The motions of the mass center of three rigid bodies at different initial positions with four boundary conditions are shown in Figs. 12(a)-12(d), respectively. We place the first rigid body near the inner wall, the second rigid body in the middle of the inner and outer walls and place the third rigid body close to the outer wall. As shown in Fig. 12, the red curve represents the motion the first rigid body, the green curve represents the second rigid body and the blue curve represents the third rigid body. As expected, the rigid body makes a spiral motion in the channel, in which the rigid body in the middle has the maximum axial speed and moves forward fastest. The degree of spiral of the rigid body motion increases with the

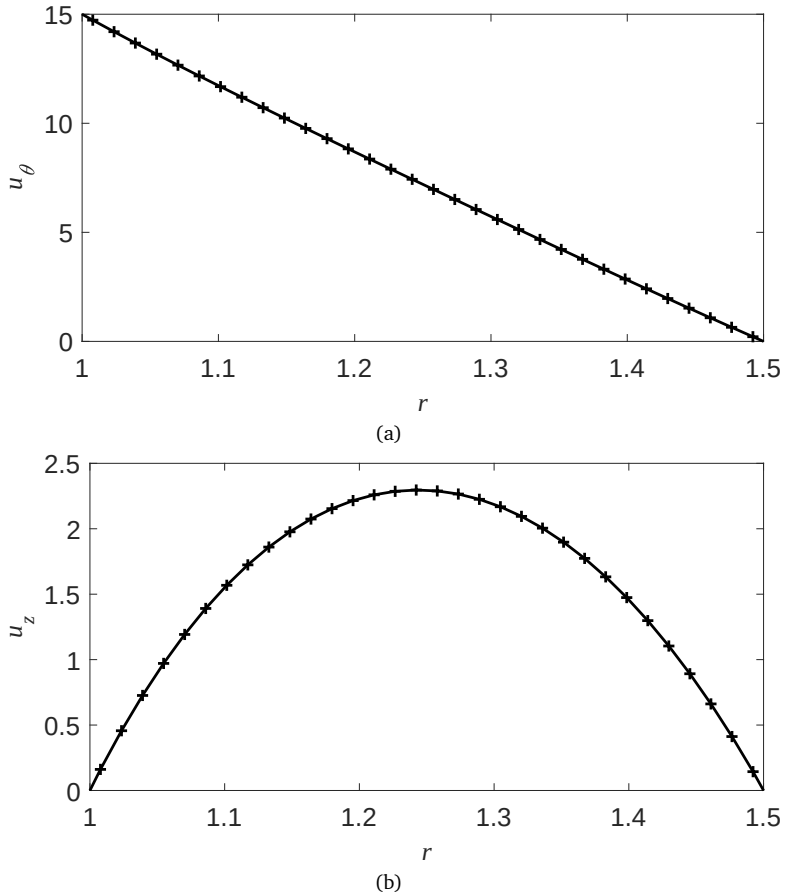

Figure 11: Fully developed flow field. (a) Annular velocity u_θ. (b) Axial velocity u_z.

increase of the circular velocity. Different rigid bodies trajectories are caused by different boundary conditions. The positions and orientations of rigid bodies and surrounding fluid velocity fields are shown at time $t = 0.1953$, 1.2891, and 2.0703 with boundary condition 3D(I) are shown in Figs. 13-15, respectively. The variation of angular velocity of the rigid body motion with boundary condition 3D(I) is shown in Fig. 16, where $\omega_p 1$ denotes the rotational angular velocity of the rigid body relative to the $\vec{r}$ axis, $\omega_p 2$ denotes the rotational angular velocity of the rigid body relative to the $\vec{\theta}$ axis, and $\omega_p 3$ denotes the rotational angular velocity of the rigid body relative to the $\vec{z}$ axis. According to the Eqs. (2.3)-(2.4), the angular velocity of the rigid body is not only related to the average value of the angular velocity of the fluid, but also related to the torque we introduced at the center of the rigid body. When the rigid body is close to another rigid body or the rigid body is close to the wall, the rotation angular velocity will have a sudden change, and the effect of this sudden change between the two rigid bodies is to make the rigid body turn a certain angle so as to avoid the overlap of the occupied area, which is the effect of the collision strategy that we adopt.

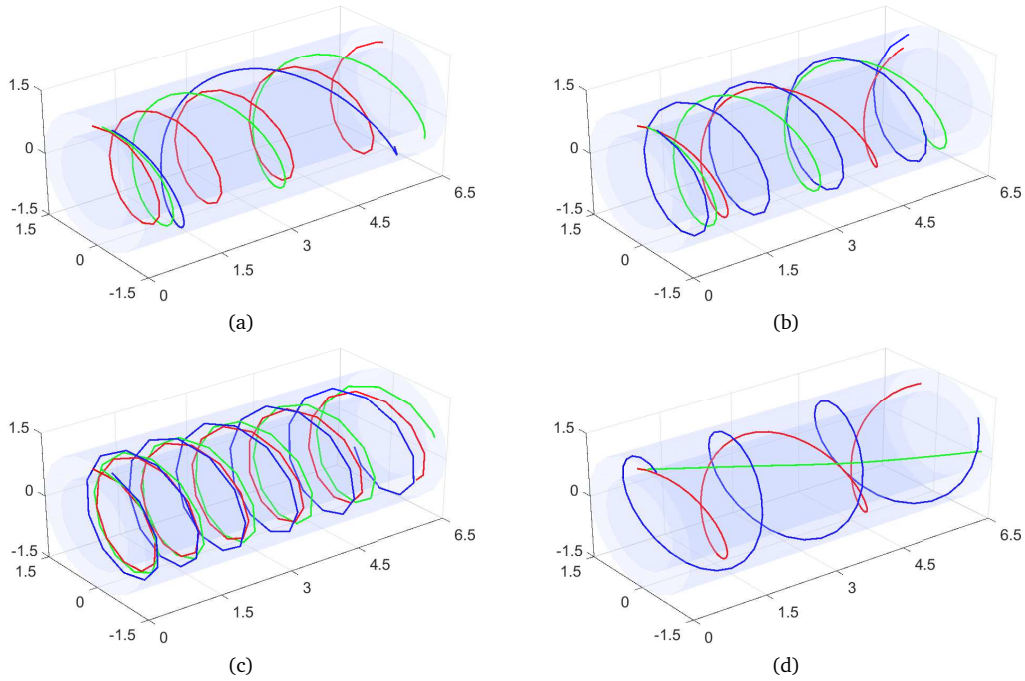

Figure 12: Motion of mass center of three rigid bodies at different initial positions with four different boundary conditions. (a) Boundary condition 3D(I). (b) Boundary condition 3D(II). (c) Boundary condition 3D(III). (d) Boundary condition 3D(IV).

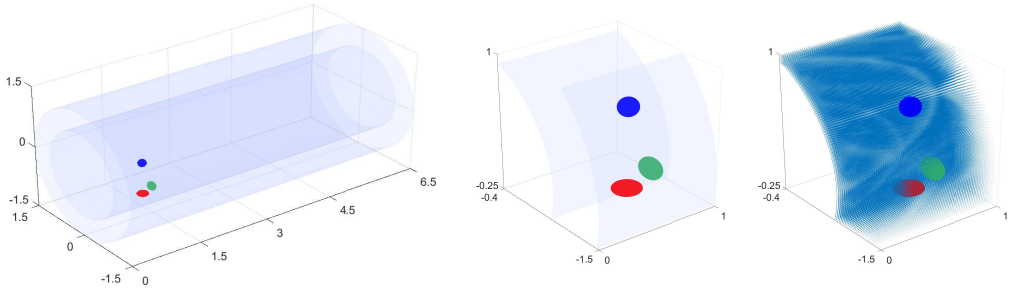

Figure 13: Position and orientation of rigid bodies and surrounding flow field, $t = 0.1953$.

Finally, we give the numerical simulation of many rigid bodies advancing in the flow field. The positions and orientations of the rigid bodies at different time are demonstrated in Fig. 17, which shows two cases with two different initial conditions. It is observed that if the rigid bodies are arranged irregularly initially, they are presented more irregularly in the rotational extrusion flow with time evolution. If the particles are arranged in order initially, they will move forward regularly in rotational extrusion flow with time increasing. It is not difficult to observe from these results that the rotating-extrusion rheometer can regulate the arrangement of particles according to fluid-particle interaction. The initial arrangement of particles can greatly affect the motions of them.

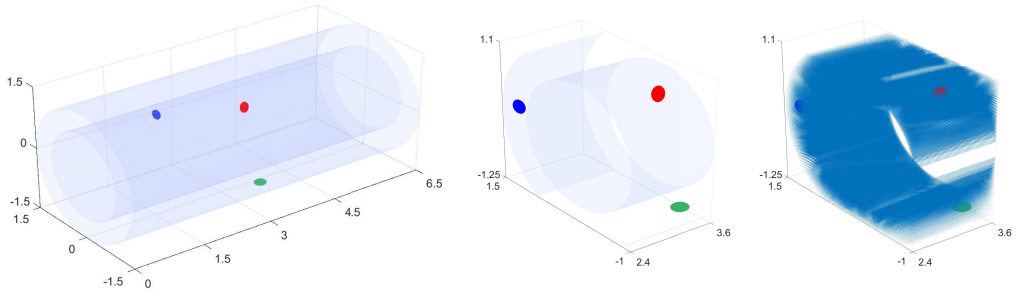

Figure 14: Position and orientation of rigid bodies and surrounding flow field, $t = 1.2981$.

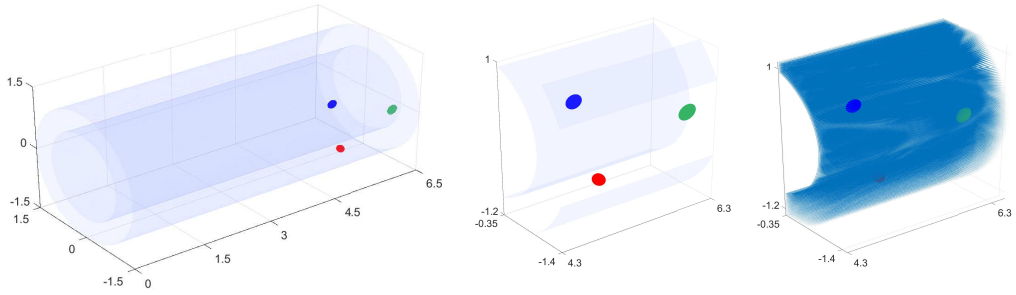

Figure 15: Position and orientation of rigid bodies and surrounding flow field, $t = 2.0703$.

4. Conclusion

In this paper, we use FPD method to simulate the fluid-solid interaction problem. We solve the coupled system in polar coordinates and cylindrical coordinates. We use a finite difference discretization in staggered MAC mesh and a pressure stabilized scheme in time. Firstly, we obtain the numerical solution of the power-law fluid driven by the Dirichlet boundary in the annular region. The comparison between the numerical solution and the analytical solution verifies the reliability of the solver for Navier-Stokes equation. For the interaction between particle and fluid, we present drag coefficient calculation for circular particle and Jeffery orbit simulation for elliptical particle to validate our fluid structure coupling solver. Then, we extend the computational domain to a three-dimensional finite hollow cylinder. We obtain the stable spiral motion of several ellipsoidal rigid bodies under the complex boundary conditions of circumferential rotation and axial drag. Finally, we show the numerical simulations of many rigid particles advancing in the fluid field. It is observed that FPD method has reliable and efficient performance for numerical simulation of fluid-solid interaction in cylindrical coordinates. In the future, we will generate our simulation in parallel computing with large scale particles. We will also consider more complex fluid-solid interaction, where solid moves more intricately than rigid motion.

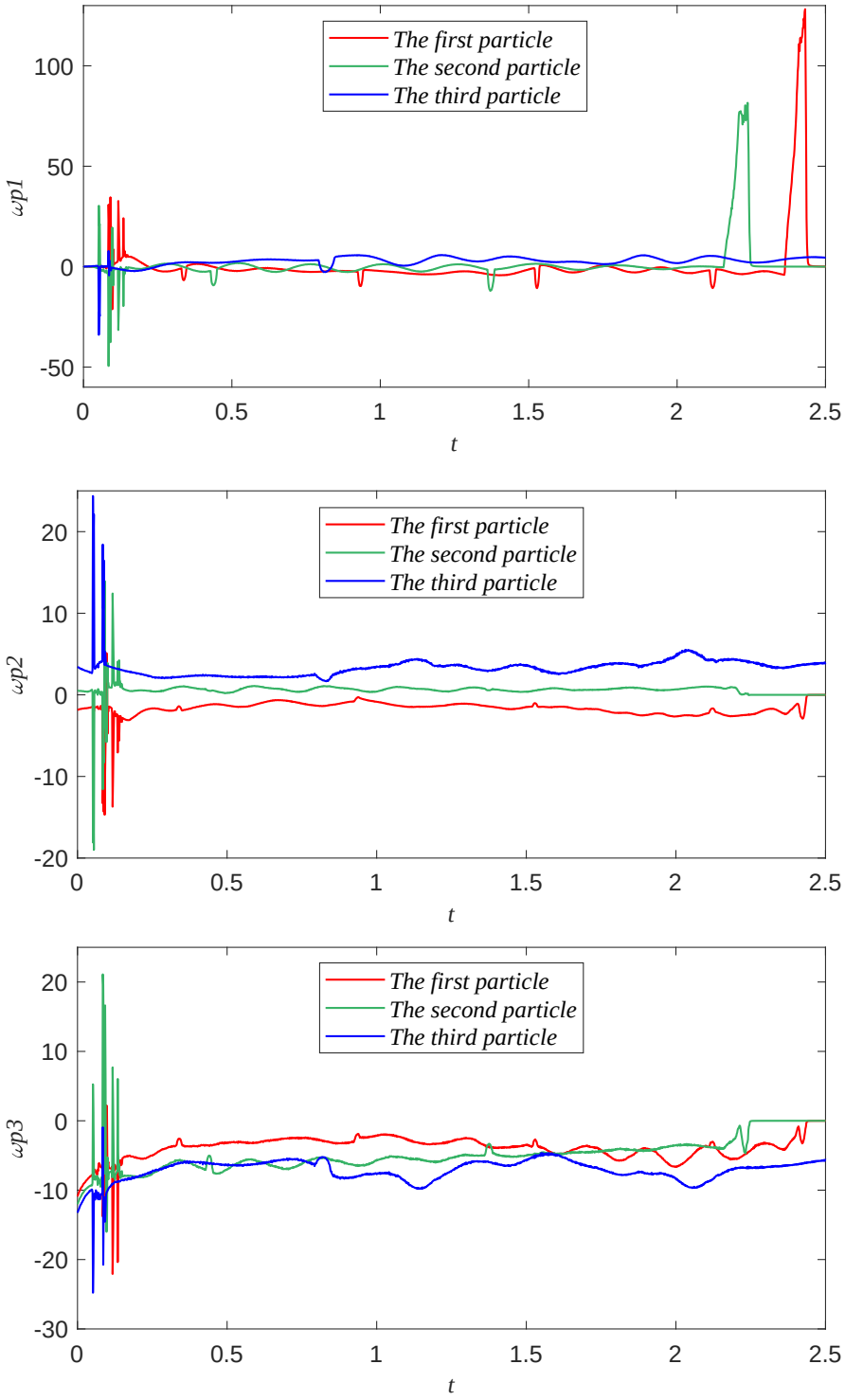

Figure 16: Angular velocity of rotation of rigid body around $\vec{r}, \vec{\theta}$ and $\vec{z}$ axes with boundary condition 3D(I).

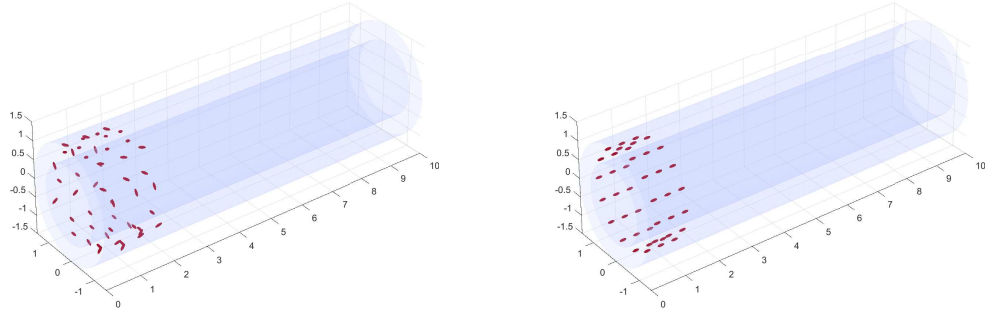

Case (I), t=0.0002 Case (II), t=0.0002

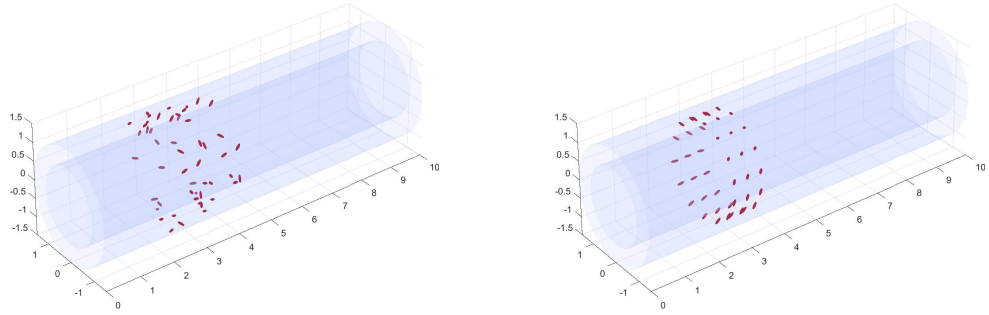

Case (I), t=0.24 Case (II), t=0.216

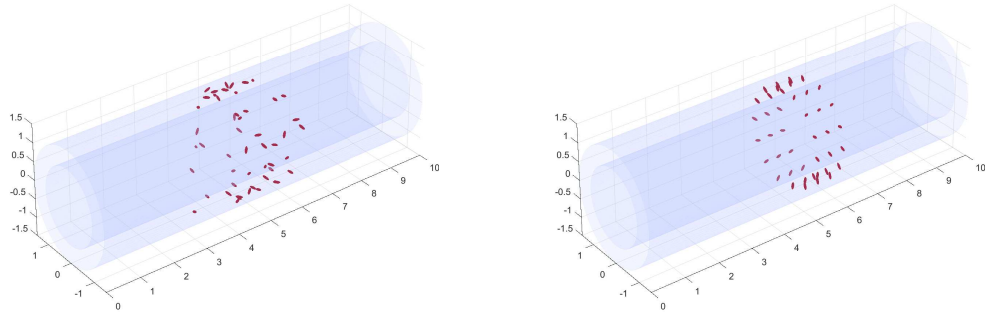

Case (I), t=0.408 Case (II), t=0.432

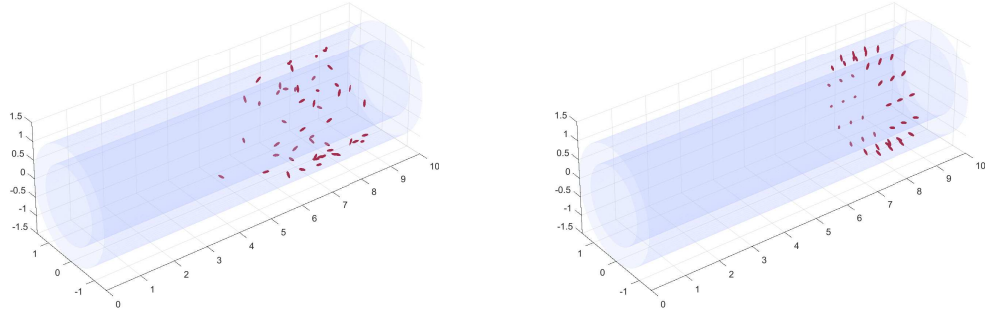

Case (I), t=0.6 Case (II), t=0.624

Figure 17: Positions and orientations of rigid bodies with two different initial arrangements at different time.

Appendix A. Definition of repulsive force and torque

For the repulsive force $\mathbf{F}_j$ and torque $\mathbf{T}_j$, we have

$$\mathbf{F}_j = \sum \mathbf{F}_j^{\mathrm{w}} + \sum_{\substack{i=1 \\ i\neq j}}^{N} \mathbf{F}_{j,i}^{\mathrm{p}},$$
$$\mathbf{T}_j = \overrightarrow{\mathbf{G}_j \vec{x}} \times \mathbf{F}_j.$$

For the particle-particle repulsive force, we define

$$\mathbf{F}_{j,i}^{\mathrm{p}} = \begin{cases} 0, & d_{j,i} > R_j + R_i + \rho, \\ \dfrac{1}{\epsilon_{\mathrm{p}}}\left(\mathbf{G}_j - \mathbf{G}_i\right)\left(R_j + R_i + \rho - d_{j,i}\right)^2, & d_{j,i} \le R_j + R_i + \rho, \end{cases}$$

where R_j is the radius of the j-th particle, $d_{j,i} = |\mathbf{G}_j - \mathbf{G}_i|$ is the distance between the centers of the j-th particle and i-th particle, ρ is the force range, and ϵ_{p} is a small positive parameter. For the particle-wall repulsive force, we define

$$\mathbf{F}_j^{\mathrm{w}} = \begin{cases} 0, & d_j' > 2R_j + \rho, \\ \dfrac{1}{\epsilon_{\mathrm{w}}}\left(\mathbf{G}_j - \mathbf{G}_j'\right)\left(2R_j + \rho - d_j'\right)^2, & d_j' \le 2R_j + \rho, \end{cases}$$

where, ϵ_{w} is another small positive parameter, and $d_j' = |\mathbf{G}_j - \mathbf{G}_j'|$ is the distance between the centers of the j-th particle and the imaginary particle as shown in Fig. 18.

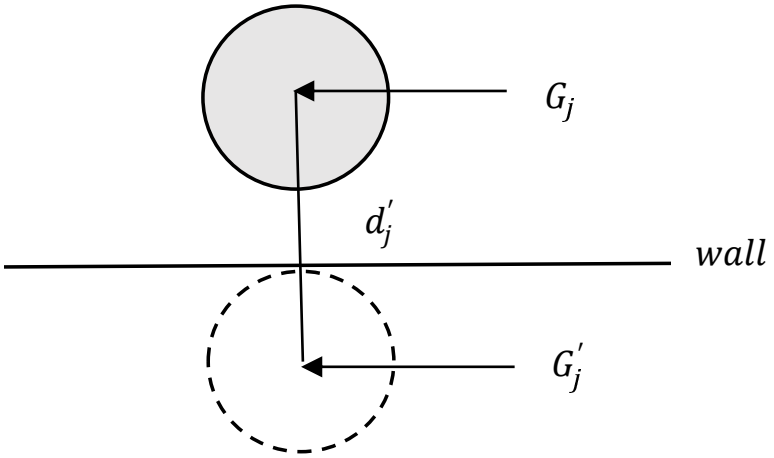

Figure 18: Imaginary particle.

Appendix B. Spatial discretization of differential operators

The second-order interpolations are used for variables evaluated at different grid points. For variables (denoted by u) solved on $(i+1/2, j, k)$, we have

$$u_{i,j,k} = \frac{u_{i+1/2,j,k} + u_{i-1/2,j,k}}{2},$$
$$u_{i+1/2,j+1/2,k} = \frac{u_{i+1/2,j+1,k} + u_{i+1/2,j,k}}{2},$$
$$u_{i+1/2,j,k+1/2} = \frac{u_{i+1/2,j,k+1} + u_{i+1/2,j,k}}{2}.$$

Similar calculations are used for variables on $(i, j+1/2, k)$ and $(i, j, k+1/2)$. For variables (denoted by u) solved on (i, j, k), the interpolation on the top boundary, right boundary and corner point are defined as follows:

$$u_{i+1/2,j,k} = \frac{u_{i+1,j,k} + u_{i,j,k}}{2}, \quad u_{i,j+1/2,k} = \frac{u_{i,j+1,k} + u_{i,j,k}}{2}, \quad u_{i,j,k+1/2} = \frac{u_{i,j,k+1} + u_{i,j,k}}{2},$$
$$u_{i+1/2,j+1/2,k+1/2} = \frac{u_{i,j,k} + u_{i+1,j,k} + u_{i,j+1,k} + u_{i,j,k+1}}{8} + \frac{u_{i+1,j+1,k} + u_{i,j+1,k+1} + u_{i+1,j,k+1} + u_{i+1,j+1,k+1}}{8}.$$

Typical finite-difference approximations to derivatives are given as

$$\nabla u_{i+1/2,j,k} = \frac{u_{i+1,j,k} - u_{i,j,k}}{\Delta r}, \quad \nabla u_{i,j+1/2,k} = \frac{u_{i,j+1,k} - u_{i,j,k}}{r_i \Delta\theta}, \quad \nabla u_{i,j,k+1/2} = \frac{u_{i,j,k+1} - u_{i,j,k}}{\Delta z},$$
$$\Delta u_{i,j,k} = \frac{r_{i+1/2}(u_{i+1,j,k} - u_{i,j,k}) - r_{i-1/2}(u_{i,j,k} - u_{i-1,j,k})}{r_i \Delta r^2} + \frac{u_{i,j+1,k} - 2u_{i,j,k} + u_{i,j-1,k}}{r_i^2 \Delta\theta^2} + \frac{u_{i,j,k+1} - 2u_{i,j,k} + u_{i,j,k-1}}{\Delta z^2},$$
$$\Delta u_{i+1/2,j,k} = \frac{r_{i+1}(u_{i+3/2,j,k} - u_{i+1/2,j,k}) - r_i(u_{i+1/2,j,k} - u_{i-1/2,j,k})}{r_{i+1/2} \Delta r^2} + \frac{u_{i+1/2,j+1,k} - 2u_{i+1/2,j,k} + u_{i+1/2,j-1,k}}{r_{i+1/2}^2 \Delta\theta^2} + \frac{u_{i+1/2,j,k+1} - 2u_{i+1/2,j,k} + u_{i+1/2,j,k-1}}{\Delta z^2},$$
$$\Delta u_{i,j+1/2,k} = \frac{r_{i+1/2}(u_{i+1,j+1/2,k} - u_{i,j+1/2,k}) - r_{i-1/2}(u_{i,j+1/2,k} - u_{i-1,j+1/2,k})}{r_i \Delta r^2} + \frac{u_{i,j+3/2,k} - 2u_{i,j+1/2,k} + u_{i,j-1/2,k}}{r_i^2 \Delta\theta^2} + \frac{u_{i,j+1/2,k+1} - 2u_{i,j+1/2,k} + u_{i,j+1/2,k-1}}{\Delta z^2},$$
$$\Delta u_{i,j,k+1/2} = \frac{r_{i+1/2}(u_{i+1,j,k+1/2} - u_{i,j,k+1/2}) - r_{i-1/2}(u_{i,j,k+1/2} - u_{i-1,j,k+1/2})}{r_i \Delta r^2}$$

$$+\frac{u_{i,j+1,k+1/2}-2u_{i,j,k+1/2}+u_{i,j-1,k+1/2}}{r_i^2\Delta\theta^2}+\frac{u_{i,j,k+3/2}-2u_{i,j,k+1/2}+u_{i,j,k-1/2}}{\Delta z^2}.$$

Acknowledgments

This research is supported in part by the National Natural Science Foundation of China (Grants 11971020, 52273038).

References

[1] T. Cebeci, J.P. Shao, F. Kafyeke and E. Laurendeau, *Computational fluid dynamics for engineers: From panel to Navier-Stokes methods with computer programs*, Springer, 10–17 (2005).
[2] S. Chandran et al., *Processing pathways decide polymer properties at the molecular level*, Macromolecules **52**, 7146–7156 (2019).
[3] S.H. Cho, H.G. Choi and J.Y. Yoo, *Direct numerical simulation of fluid flow laden with many particles*, Int. J. Multiph. Flow. **31**, 435–451 (2005).
[4] A. Furukawa, M. Tateno and H. Tanaka, *Physical foundation of the fluid particle dynamics method for colloid dynamics simulation*, Soft Matter **14**, 3738–3747 (2018).
[5] R. Glowinski, *Finite element methods for incompressible viscous flow*, Handb. Numer. Anal. **9**, 3–1176 (2003).
[6] R. Glowinski, T.W. Pan, T.I. Hesla and D.D. Joseph, *A distributed Lagrange multiplier/fictitious domain method for particulate flows*, Int. J. Multiph. Flow. **25**, 755–794 (1999).
[7] R. Glowinski, T.W. Pan, T.I. Hesla, D.D. Joseph and J. Périaux, *A distributed Lagrange multiplier/fictitious domain method for flows around moving rigid bodies: Application to particulate flow*, Int J Numer Methods Fluids **30**, 1043–1066 (1999).
[8] R. Glowinski, T.W. Pan and J. Périaux, *A fictitious domain method for external incompressible viscous flow modeled by Navier-Stokes equations*, Comput Methods Appl Mech Eng **112**, 133–148 (1994).
[9] M. Gao and X.P. Wang, *An efficient scheme for a phase field model for the moving contact line problem with variable density and viscosity*, J. Comput. Phys. **272**, 704–718 (2014).
[10] Z. Guo and T.S. Zhao, *Explicit finite-difference lattice Boltzmann method for curvilinear coordinates*, Phys. Rev. E **67**, 066709 (2003).
[11] F.H. Harlow and J.E. Welch, *Numerical calculation of time-dependent viscous incompressible flow of fluid with free surface*, The Phys. Fluids **8**, 2182–2189 (1965).
[12] H.H. Hu, *Direct simulation of flows of solid-liquid mixtures*, Int. J. Multiph. Flow. **122**, 335–352 (1996).
[13] H.H. Hu, D.D. Joseph and M.J. Crochet, *Direct simulation of fluid particle motions*, Theor Comp Fluid Dyn **3**, 285–306 (1992).
[14] G.B. Jeffery, *The motion of ellipsoidal particles immersed in a viscous fluid*, Proc. R. Soc. Lond. A. **102**, 161–179 (1922).
[15] H. Johnston and J.G. Liu, *Accurate, stable and efficient Navier-Stokes solvers based on explicit treatment of the pressure term*, J. Comput. Phys. **199**, 221–259 (2004).
[16] B. Kim, C.B. Chang, S.G. Park and H.J. Sung, *Inertial migration of a 3D elastic capsule in a plane Poiseuille flow*, Int J Heat Fluid Flow **54**, 87–96 (2015).
[17] Y.J. Li, X.Y. Wen, M. Nie and Q. Wang, *Toward subtle manipulation of fine dendritic β-nucleating agent in polypropylene*, ACS omega **2**, 7230–7238 (2017).

[18] P. Mendis, T. Ngo, N. Haritos, A. Hira, B. Samali and J. Cheung, *Wind loading on tall buildings*, Electron. J. Struct. Eng. (2007).
[19] A. Nourbakhsh, S. Mortazavi and Y. Afshar, *Three-dimensional numerical simulation of drops suspended in Poiseuille flow at non-zero Reynolds numbers*, Phys. Fluids. **23**, 123303 (2011).
[20] T.W. Pan, C.C. Chang and R. Glowinski, *On the motion of a neutrally buoyant ellipsoid in a three-dimensional Poiseuille flow*, Comput Methods Appl Mech Eng **197**, 2198–2209 (2008).
[21] B.F. Spencer and M.K. Sain, *Controlling buildings: A new frontier in feedback*, IEEE Control Syst **17**, 19–35 (1997).
[22] M.E. Staben and R.H. Davis, *Particle transport in Poiseuille flow in narrow channels*, Int. J. Multiph. Flow. **31**, 529–547 (2005).
[23] Z. Tadmor and C.G. Gogos, *Principles of Polymer Processing*, John Wiley & Sons (2006).
[24] H. Tanaka and T. Araki, *Simulation method of colloidal suspensions with hydrodynamic interactions: Fluid particle dynamics*, Phys. Rev. Lett. **85**, 1338 (2000).
[25] H. Tanaka and T. Araki, *Viscoelastic phase separation in soft matter: Numerical-simulation study on its physical mechanism*, Chem. Eng. Sci. **61**, 2108–2141 (2006).
[26] R.J.R. vander Meûlen, *The immersed boundary method for the (2D) incompressible Navier-Stokes equations*, MAS. 1–126 (2006).
[27] E.J. Weinberg, D. Shahmirzadi and M.R.K. Mofrad, *On the multiscale modeling of heart valve biomechanics in health and disease*, Biomech Model Mechanobiol **9**, 373–387 (2010).
[28] S. Yamanaka, A. Furukawa and H. Tanaka, *Complex dynamical interplay between solid particles and flow in driven granular suspensions*, Phys. Rev. E. **100**, 012907 (2019).
[29] J. Zhang, X. Xu and T. Qian, *Anisotropic particle in viscous shear flow: Navier slip, reciprocal symmetry, and Jeffery orbit*, Phys. Rev. E. **91**, 033016 (2015).